Applied Physics A (2023) 129:453
https://doi.org/10.1007/s00339-023-06713-y

Applied Physics A
Materials Science & Processing

Structural, plasmonic and electronic properties of zirconium carbonitride thin films prepared by dual ion beam deposition

Tingting Liu[1] · Yujing Ran[2] · Tianrun Wang[1] · Xiaoting Yu[1] · Guangxiao Hu[1] · Zhaotan Jiang[1] · Zhi Wang[1]

Received: 19 November 2022 / Accepted: 10 May 2023 / Published online: 31 May 2023
© The Author(s), under exclusive licence to Springer-Verlag GmbH, DE part of Springer Nature 2023

Abstract

Metal carbonitride is a new type of tunable plasmonic materials and can be tuned by nitrogen and carbon content. In this work, zirconium carbonitride (ZrC_xN_y) thin films are prepared by dual ion beam deposition. The effects of C content and assisting ions on the structure and plasmonic properties of the films are studied. The results show that all the films are in B1-structure. C content increasing can reduce the shielding plasma frequency $\hbar\omega_c$ and the carrier concentration of the film. Appropriate assisting ion beam energy E_a and current density J_a can promote the crystallinity of the film. As E_a and J_a increases, $\hbar\omega_c$ increases initially and then decreases. The effects of the assisting ions can be attributed to the C content and the C-related defects, which is confirmed by the calculation of electronic states. The calculated density of state of the electrons shows that increasing C-substitute defects can decrease the threshold energy of interband transition, and the interstitial C defects lead to the similar effect. The study shows that metal carbonitride is a more tunable plasmonic material in visible and infrared region, and can also be modulated by the assisting ions.

Keywords Zirconium carbonitride · Thin films · Assisting ions · Plasmonic · Electronic structure

1 Introduction

In recent years, surface plasmon has been used in medical treatment [1, 2], photovoltaic devices [3], energy storage [4], optical fiber [5], sub-wavelength communication devices and surface coating [6, 7], and become one of the hot research areas of nano photonics [8–10]. Among plasmonic materials, gold and silver were favored because of their good stability, high negative permittivity, and low loss [11, 12]. However, their poor adjustability, high cost, and low melting point limit the practical application of gold and silver [13–17]. Therefore, it is necessary to find alternative plasmonic materials applied in some fields.

B1-structured transition metal nitrides have been regarded as an attractive plasmonic materials, owing to their excellent thermal stability and tunable optical properties from ultraviolet to infrared light [18]. Among them, TiN is the most widely studied [14, 16, 19, 20], and has been widely used in optical hyperbolic materials [21], perfect absorbers [22], sensor chips [23], and other fields. Other binary nitrides, mainly ZrN [24–27], have received increasing attention to meet various demands. Additionally, ternary nitride compounds have attracted more and more attention. Advantages that binary nitride could not reach have been obtained [28–31] in ternary nitride. By doping element and doping content, we can modulated the plasmonic properties of the materials in a wider region. Ternary nitride is usually metal-doped by alloying different metal in nitridization. Most of the nonmetal-doped ternary nitride are metal oxynitride [32–35]. In fact, carbon-doping is an effective way to get various properties and applications for nitride. Metal carbonitride is an effective coating for surface modification to promote the hardness and resistance to corrosion [36, 37]. Researchers prepared a series of metal carbide and ternary XCN (X = Ti, Zr) to study their properties [38–41].

Tingting Liu and Yujing Ran contributed equally to this work.

✉ Yujing Ran
ranyujing@ustb.edu.cn

✉ Zhi Wang
wangzhi@bit.edu.cn

[1] School of Physics, Beijing Institute of Technology, No. 5, South Street, Zhongguancun, Beijing 100081, People's Republic of China

[2] School of Chemistry and Biological Engineering, Basic Experimental Center for Natural Science, University of Science and Technology Beijing, No. 30, Xueyuan Road, Beijing 100083, People's Republic of China

About the optical and plasmonic properties of binary metal carbide, the materials are usually in MAX structure [42–44]. However, the plasmonic properties of cubic ternary XCN have not been studied extensively.

Most of the ZrCN samples reported so far are prepared by chemical vapor deposition [41], cathode arc deposition [38] and magnetron sputtering [39]. In this work, ZrC_xN_y films are prepared by dual ion beam deposition (DIBD), in which the growing films are bombarded by an assisting ion beam. The energy and current of the assisting ions can be used to affect the structure and characteristics of the deposited films. So DIBD gives more ways to modulate and optimize the properties of films.

In this work, the effect of carbon content and assisting ions on the crystal structural and plasmonic properties of the prepared films is investigated experimentally. The electronic states were studied by first-principle calculation to explain the experimental results. The results show that ZrC_xN_y is a potential tunable and applicable plasmonic materials in visible to infrared region, and DIBD is an effective method to prepare and modulated the plasmonic XCN films.

2 Experimental details

ZrC_xN_y thin films were prepared by a DIBD system, the schematic diagram of which is shown in Fig. 1. There are two Kaufman ion sources in this system, one of which serves as a sputtering source (ϕ 8 cm) and the other as an assisting source (ϕ 6 cm). The sputtering source is placed horizontally and used to generate sputtering Ar^+ beam. The assisting ion source is placed at 45° to the horizontal direction, and used to generate the assisting ion beam. The substrate is fixed to the top of the vacuum chamber and a target is placed below the substrate.

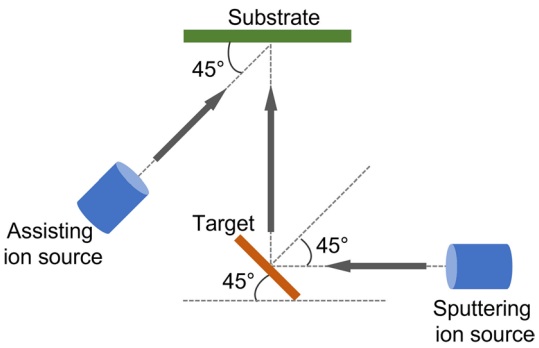

Fig. 1 Schematic diagram of DIBD system

During the deposition, Zr atoms are sputtered from a 99.99% pure Zr target by an beam of argon ions. All films are deposited on $1 \times 1\, cm^2$ JGS1 SiO_2 substrates. The background vacuum pressure is 8×10^{-4} Pa and the working pressure is kept at 4.8×10^{-2} Pa. The sputtering source is injected with a flow of Ar gas of 4 sccm to generate sputtering ions. The energy and current density of the sputtering beam were set to 800 eV and 1.2 mA/cm^2. A mixed gas flow of Ar and N_2 were supplied into the assisting ion source, in which the flow rate of Ar is 2.5 sccm, and the flow rate of N_2 is a variable to get different nitrogen content in films. A flow of CH_4 gas was supplied to the chamber to get the carbon doping. The substrate rotates at a constant speed during deposition to ensure the uniformity of the film. The thickness of all the films is 100 ($\pm$10) nm, which is detected with a quartz crystal oscillator. All films were deposited at room temperature.

We prepared three groups of samples, the parameters of which are shown in Table 1. To study the effect of carbon doping content, we changed the partial pressure ratio of CH_4 *r*. *r* was set to 0/0.17/0.33/0.67/1.0, and the total flow rate of CH_4 and N_2 was keep constant of 3 sccm. The effect of assisting ion energy E_a and current density J_a were studied with *r* set at 0.17 in the other two groups. E_a was different and J_a was kept stable at 0.3 mA/cm^2 in one group. While in the other group, J_a was different and E_a was maintained at 300 eV. As a contrast, a thin film was prepared without assisting ion bombardment ($E_a = 0$, $J_a = 0$) under the same condition.

The elemental composition of the film was determined by an energy X-ray dispersive spectroscopy (EDS) on a scanning electron microscope (SEM, Zeiss, SUPRA55) system under a vacuum of 1.0×10^{-8} Pa. The crystal structure of the films were investigated by X-ray diffraction (XRD) with Cu–Kα_1 radiation ($\lambda = 0.15406$ nm) as the diffraction source. The plasmonic properties of thin films are mainly reflected by the complex permittivity, which was measured by spectroscopic ellipsometry (smart SE 850 DUV) with an incident

Table 1 Experimental parameters

Experimental parameters	I	II	III
Ar flow rate (sccm)	6.0	6.0	6.0
CH_4 flow rate (sccm)	0/0.5/1.0/2.0/3.0	0.5	0.5
N_2 flow rate (sccm)	3.0/2.5/2.0/1.0/0	2.5	2.5
r	0/0.17/0.33/0.66/1.0	0.17	0.17
E_a (eV)	300	0/100/200/300/500/700	300
J_a (mA/cm^2)	0.3	0.3	0.2/0.3/0.4/0.5/0.6/0.7

angle of 70°. All measurements were performed at room temperature.

3 Results and discussion

3.1 Effects of carbon doping

Table 2 shows the atomic composition of the ZrC_xN_y film deposited with different CH_4 flow ratio r. It can be seen that both the ZrN_x and the ZrC_x film are metal-rich, especially ZrC_x film. The Zr content of the ZrC_xN_y film is lower than that of the binary films. As we expected, C content increases with r increasing. For the film of r=0.66, C content is lower than N content, even the CH_4 flow is higher than N_2 flow during the deposition, which is because that N atom is easier to combine with Zr atom.

Table 2 Atomic composition of the ZrC_xN_y film measured by EDS

r	C%	N%	Zr%
0	0	43.9	56.1
0.17	4.5	41.7	53.8
0.33	7.8	40.7	51.5
0.66	13.9	36.8	49.3
1.0	34.7	0	65.3

Figure 2 shows the AFM images of the films deposited with different r. It can be seen that as r increases, the film becomes smoother. The roughness (R_a) of the films is 0.63, 0.62, 0.55, 0.43, and 0.37 nm for the films of r=0, 0.17, 1.33, 0.67, and 1, respectively. Roughness is related to grain size. The grains in the films prepared with higher r are smaller, which is consistent with the following XRD results. The AFM results reflect that N_2 is easier to combine and crystalize with Zr atoms than CH_4.

Figure 3a shows the XRD patterns of the films deposited with different r. The analysis of the XRD was based on JCPDS cards (35-0784 and 35-0753). The XRD results show that all the films are in B1-structure. The films have characteristic diffraction peaks of (111) and (200), and (200) peak is much weaker than (111) peak. So the films can be regarded as mainly (111)-oriented. The (111) characteristic diffraction peaks are located between the fcc-ZrC (111) peak and the fcc-ZrN (111) peak. With r increasing, the (111) peak gradually move towards ZrC (111), and the (200) peak shows similar behavior. No diffraction peak of other chemical phase appears, which indicates that in carbon-doped zirconium nitride, C atoms enter or fill the voids in the ZrN lattice, and even the N atoms in the original ZrN lattice will be replaced by C atoms. That is to say, the defects caused by carbon doping mainly exist in the form of various point defects. ZrN and ZrC are both

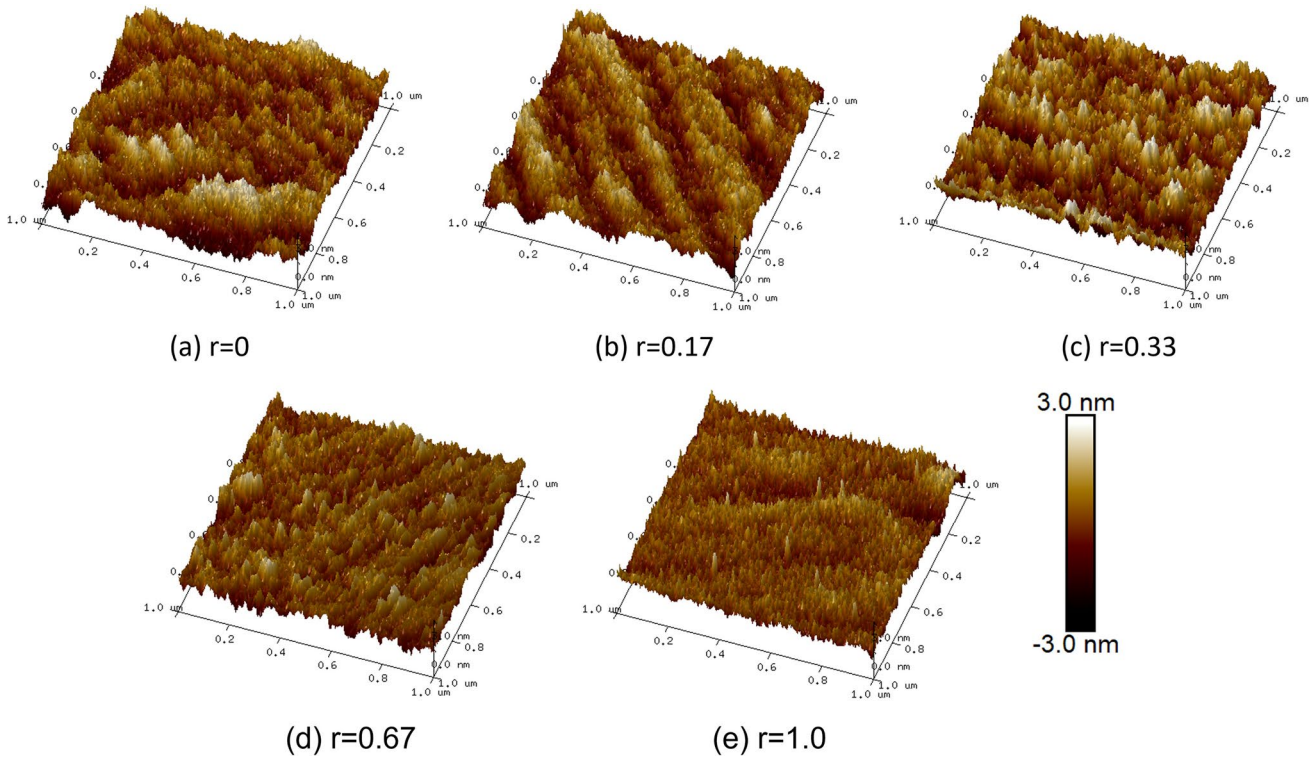

Fig. 2 1 μm × 1 μm AFM images of ZrC_xN_y films prepared at different CH_4 partial pressure ratio r

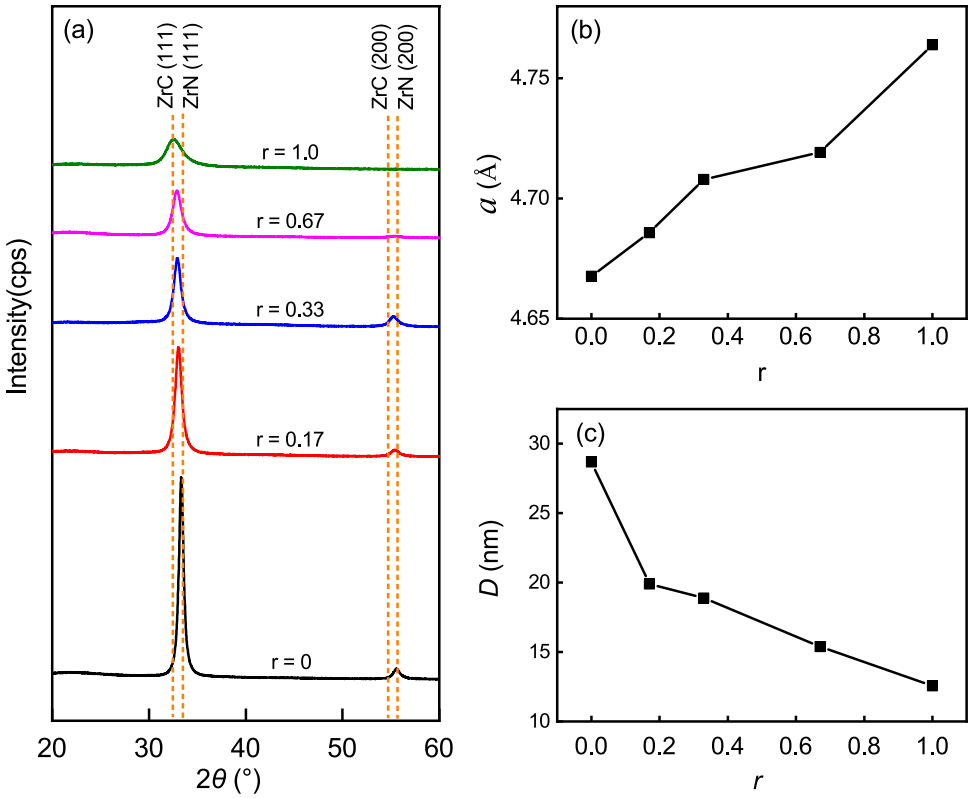

Fig. 3 XRD pattern (**a**), lattice constant (**b**) and grain size (**c**) of ZrC_xN_y films prepared at different CH_4 partial pressure ratio r

B1-structured, and the radius of N atom and C atom is very close. Therefore, according to Hume-Rothery rule [45], ZrC_xN_y film can easily form a solid solution of cubic ZrN_x and ZrC_x, in which the distribution of N atoms and C atoms has a certain uniformity. The final preferred orientation of thin films is the result of growth competition among grains with different alignment, and (111) alignment is obviously dominant in grain growth.

Figure 3b shows the lattice constants a of ZrC_xN_y films calculated by the Bragg equation. It can be seen that the lattice constant of ZrC_xN_y increases with r in the range of 4.66–4.77 Å, which is due to that a Zr–C bond is longer than a Zr–N bond.

The crystallinity of the film can also be reflected by grain size. Based on the full width at half maximum β of the (111) peak, the grain size D was calculated with Scherrer equation:

$$D = 0.9\lambda/\beta\cos\theta. \quad (1)$$

The D values in Fig. 3c shows that the grain size of the film is 28.7 nm without C doping, but decreases sharply to about 16 nm with r increasing. The grain size of ZrC_x is only about 12.6 nm. In fact, the crystallization of ZrC_x is more difficult than that of ZrN_x in the physical vapor phase deposition owing to the weaker oxidizability of C atoms. C atoms may replace the N atoms, and fill the interstitial space, and so prevent the crystallization and growth of grain.

Permittivities are the basis for the plasma materials. The permittivity of the films were determined by ellipsometry with an incident angle of 70°. The complex permittivity $\varepsilon = \varepsilon_1 + i\varepsilon_2$ is determined by the measured ellipsometric angles Ψ and Δ, and then fitted to Drude–Lorentz model with two Lorentz factors.

Figure 4 shows the complex permittivity of the films prepared at different CH_4 flow rate r. Figure 4a describes the real part ε_1 of the permittivity varying with the wavelength. For ZrC_xN_y films, the curves are positive at short wavelengths and negative at long wavelengths. This means that as the wavelength increases, the film turns from dielectric to metallic. In the range of negative ε_1 0, with the same λ, the larger r is, the smaller the absolute value of ε_1 is, and the less metallic the film is. The real part of permittivity of ZrC film ($r = 1.0$) exhibits a double near zero dielectric property in 200–900 nm, in which, ε_1 transforms from dielectric to metallic and then to dielectric. The double near zero characteristics of the ZrC thin film possibly originates from the interband and intraband transition of electronic state, as reported in NbN [46], nonstoichiometric defects can also lead to different ENZ behavior.

Usually the frequency where permittivity crosses zero (ε_1=0) is used to define the screened plasma frequency, under which the total valence electron is partly shielded[47, 48]. Figure 4b shows the corresponding energy value $\hbar\omega_c$ of the ZrC_xN_y when ε_1=0. Obviously, as r increases, $\hbar\omega_c$

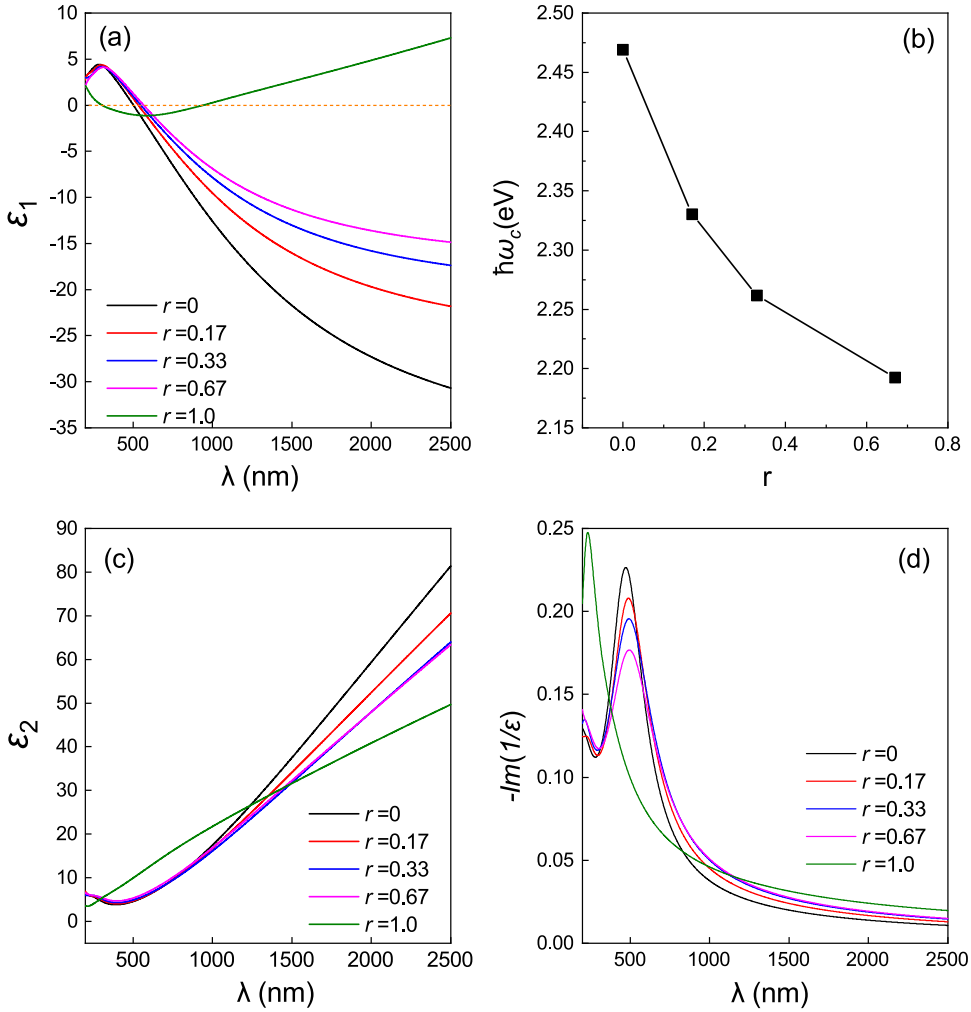

Fig. 4 Results of permittivity of the films at different CH_4 partial pressure ratio r. **a** Real part ε_1; **b** $\hbar\omega_c$ values corresponding to ε_1=0; **c** imaginary part ε_2; (**d**): energy loss function

decreases. The behavior of ω_c directly reflects the change of carrier concentration n, because ω_c is directly proportional to plasma frequency ω_{ps}, and ω_{ps} is directly proportional to the square root of carrier concentration n, as the following relation[47, 48]

$$\omega_{ps} = \sqrt{ne^2/\varepsilon_0 m^*}. \tag{2}$$

Based on the results and the formula, it can be concluded that the carrier concentration n decreases with r, which is consistent with the previous discussion that $\hbar\omega_c$ decreases with the increase of r at a fixed wavelength.

The free electrons in the conduction band of metallic Zr atom can be absorbed by the valence band of non-metallic atoms. The valence band of carbon atoms can absorb more free electrons than nitrogen atoms. So the increasing of doping C atoms reduces the carrier concentration and the ω_c value. Additionally, the defects and grain boundary can also capture free electrons and reduce the carrier concentration, which make the films less metallic.

Figure 4c describes the imaginary part ε_2 of the permittivity. Since ε_2 is considered to be related to optical loss, it can be seen from the figure that in the near infrared region, a higher r will reduce optical loss. To further investigate the properties of the film, the energy loss of the film is calculated by the following formula [49]:

$$-Im\left(\frac{1}{\varepsilon}\right) = \frac{\varepsilon_2}{\varepsilon_1^2 + \varepsilon_2^2} \tag{3}$$

Figure 4d shows the energy loss spectra of films deposited with different r. It can be seen that the energy loss of the film decreases with C content increasing, which indicates that appropriate C doping of ZrN can effectively reduce the energy loss. With the increase of r, the peak energy loss moves slightly toward the long wavelength direction. The energy loss peak of pure ZrC is located in the ultraviolet region near 230 nm. The behavior of energy loss may be related to the interband transition.

3.2 Effects of assisting ions

Figure 5 shows the EDS results of the films as a function of assisting ion energy E_a and current density J_a. It can be seen that E_a and J_a have obvious effect on the content, especially the carbon atom content of the films. For E_a of 0–300 eV, Zr content of the films is about 50%. However, for the E_a above 300 eV, the Zr content decreases with E_a increasing. This result can be attributed to the increase of implantation of N and C atoms at higher E_a. Possibly, the optimal E_a for the combination and crystallization of ZrN is near 300 eV. So as E_a increases, N content increases initially and then decreases, and consistently, C content decreases initially and then increases. The effect of J_a on the content of the films in similar to, but much less than that of E_a.

Figure 6a shows the XRD patterns of films deposited under different E_a, in which we can see that all the films are fcc-structured. All the films show a preferred (111) orientation and some films show a weak (200) orientation. Obviously, the experimental environment is beneficial to the growth of (111) orientation of grain. The positions of characteristic peaks show that a solid solution of ZrN and ZrC formed. We can see that as E_a increases, the diffraction peak becomes stronger, but is weakened when E_a increases to 500 eV and 700 eV, which indicates that too high E_a is not conducive to crystal crystallization. Figure 6b shows the XRD patterns of the films deposited under different J_a. We can see the films still exist as a solid solution of (111)-oriented fcc-ZrN and fcc-ZrC. With J_a increasing, the diffraction peaks gradually increases, but do not change much when J_a reach 0.5 mA/cm^2. Obviously, E_a affects the crystallinity much more significantly than J_a does.

The alignment selection effect of the ions is mainly related to the preferential resputtering. The resputtering yield of assisting ions on the (111) plane is the lowest.

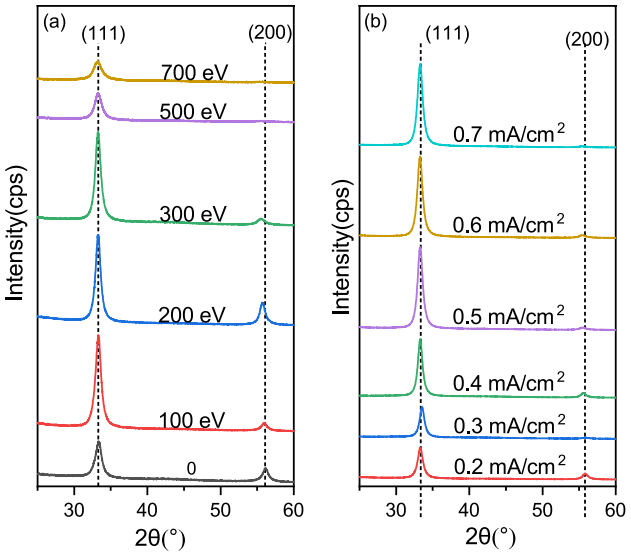

Fig. 6 XRD θ-2θ patterns of the ZrC_xN_y films prepared with different E_a (**a**) and J_a (**b**)

Since (111) orientation has a higher surface energy [25]. The crystallinity enhancement can be attributed mainly to assisting ions promoting the mobility of adatoms. The energy and momentum of the assisting ions were transported to adatoms through collision, and the surface mobility of the adatoms is enhanced consequently. But the assisting ions with energy above 500 eV can cause more defects and depress the crystallinity. To some extent, with the increasing E_a and J_a, annealing effect happened on the crystal. The effect of J_a on crystal is more similar to annealing and can promote the crystallinity. However, the effect of increasing E_a is mainly a kinetic process. High E_a with low J_a can cause significant damage to crystal through resputtering.

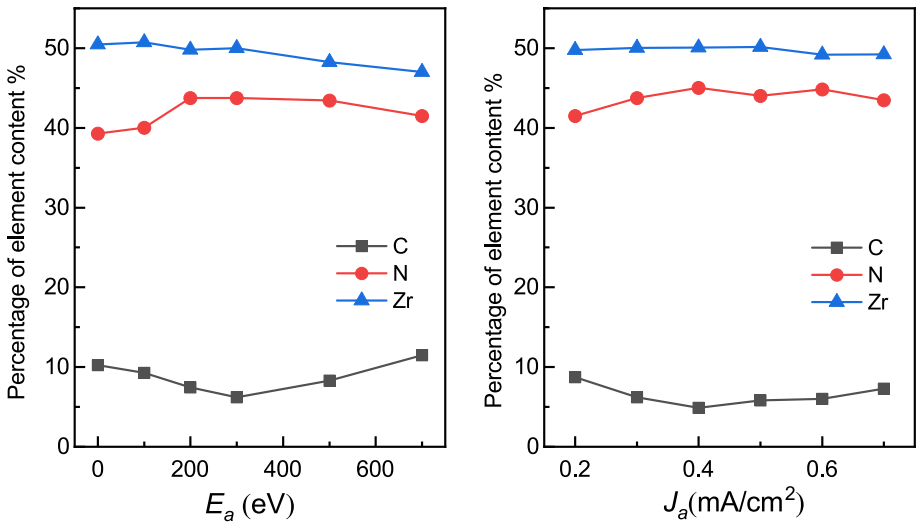

Fig. 5 Atomic composition of the films prepared with different E_a (**a**) and J_a (**b**)

Figure 7a shows the real permittivity ε_1 of ZrC_xN_y film prepared under different assisting ions. Panel (a) and (b) shows the results of ε_1 as a function of E_a and J_a respectively. The results show the film turns from dielectric to metallic as wavelength increases. The screened plasma energy $\hbar\omega_c$ values of the films are shown in Fig. 8. It can be seen that as E_a or J_a increases, $\hbar\omega_c$ increases first and then decreases. Obviously, the effect of E_a on $\hbar\omega_c$ is much more significant than that of J_a.

Figure 9 depicts the imaginary part ε_2 of ZrC_xN_y thin films prepared with different E_a and J_a. Obviously, ε_2 first decreases and then increases with the increase of wavelength. The inset depicts the details near the lowest point of ε_2. It can be seen that with the increase of E_a or J_a, the minimum of ε_2 exhibits a slight red shift.

The variation of permittivity *vs*. E_a and J_a may be contributed to the element content and defects. It can be concluded that the experimental laws of $\hbar\omega_c$ in Fig. 8 is related to those of C content in Fig. 5. As E_a or J_a increase, the $\hbar\omega_c$ and carbon content initially increase and then decrease, but C content initially decreases and then increases. Furthermore, $\hbar\omega_c$ reaches its maximum at 300 eV and 0.4 mA/cm^2 at which C content arrives at its minimum. The influence of E_a is more significant than that of J_a, because the C content fluctuates more drastically with E_a than with J_a. As discussed above, C-doping promotes valence band and makes the films less metallic, which can also be shown in the calculation of the electronic states in the following section.

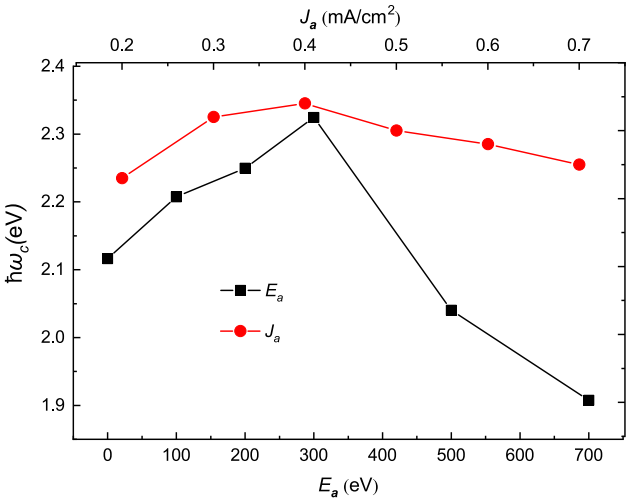

Fig. 8 The screened plasma energy $\hbar\omega_c$ (corresponding to ε_1=0) of the ZrC_xN_y films as a function of assisting ion energy E_a (**a**) and current density J_a (**b**)

4 Electronic states

The dielectric properties of the films are related to their electronic structure. To study the mechanism of carbon doping and assisting ions affecting on the dielectric properties of ZrC_xN_y films, we calculated the electronic density of states (DOS) of ZrC_xN_y by first-principles calculations. The calculations were performed using the Perdew-Burke-Ernzerhof function under generalized gradient approximation (GGA-PBE) based on the CASTEP module in Materials Studio. The cutoff energy of the plane wave was set as 310 eV, and the SCF was set as 5×10^{-7} eV/ atom.

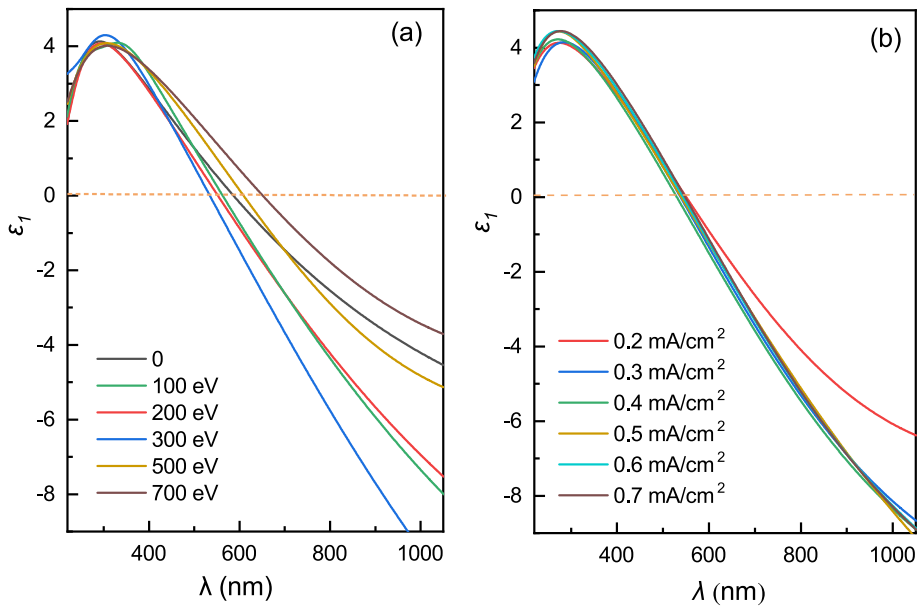

Fig. 7 Real part ε_1 of the permittivity of the ZrC_xN_y films prepared with different E_a (**a**) and J_a (**b**) as functions of wavelength

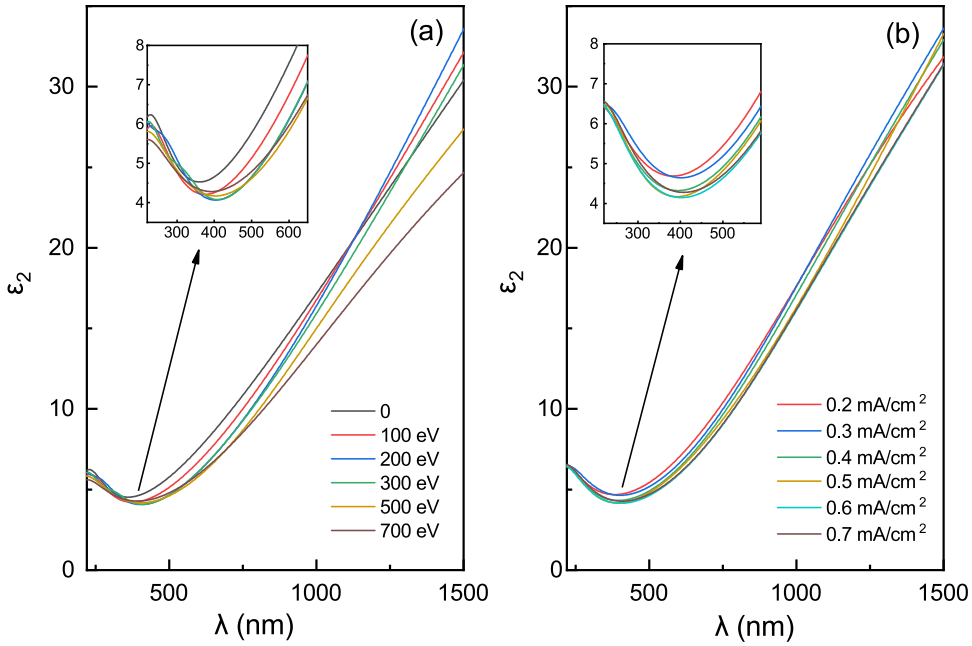

Fig. 9 Imaginary part of the permittivity ε_2 of the ZrC_xN_y films with different E_a (**a**) and J_a (**b**) as a function of wavelength

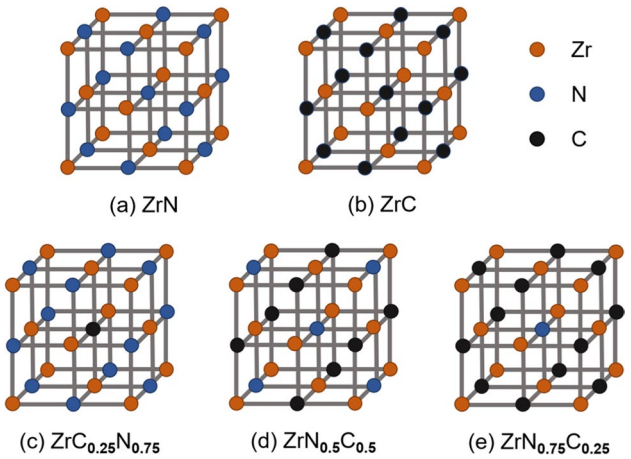

Fig. 10 Crystal cells of ZrC_xN_{1-x} with different C content x

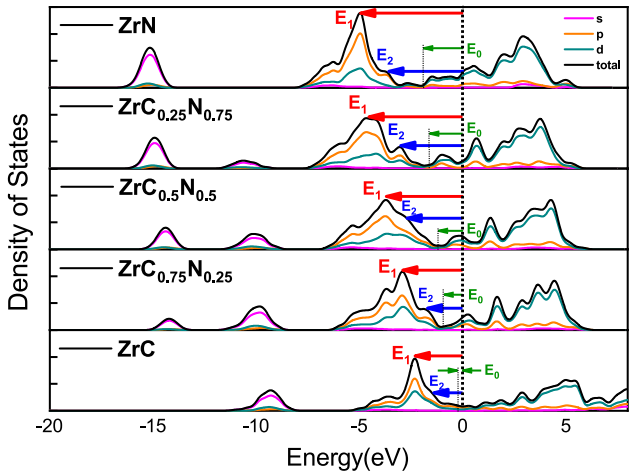

Fig. 11 Electronic density of states of ZrC_xN_y with different C doping. The Fermi level (dashed line) is set as zero

We first studied the electronic DOS of ZrC_xN_y with different C content in which only substitute doping exist. The calculation was based on crystal cells shown in Fig. 10. The lattice constants and atomic positions of ZrC_xN_{1-x} structure were optimized to make the lattice system reach the lowest energy to ensure accurate and effective calculation results.

As x in the ZrC_xN_{1-x} crystal cell gradually increases from 0 to 1, the calculated lattice constants range from 4.62 to 4.70 Å, which confirms the XRD results in Fig. 3 (4.66–4.77 Å). The calculated DOS are shown in Fig. 11. The Fermi level in the figure is set as zero. It can be seen that in the band structure of ZrN, there are three bundles of bands: N-2*s* bands around – 15 eV, hybridized bands of N-2*p* and Zr-3*p* regarded as valence bands, and the conductive Zr-4*d* bands across fermi surface, which is the main contribution of the metallic properties. It can be seen that the peak of DOS below Fermi level moves toward high energy as C content increases.

Plasmon resonance excitation is mainly due to the interaction between interband and intraband transitions [50]. The bands around the Fermi level in Fig. 11 are responsible for the metallicity (negative ε_1) in the long wavelength range. In this region, the partial coupling of the 2*p* states contributes little to absorption. At higher energy, interband transition from nonmetal 2*p* to Zr 4*d* will create a dielectric screening, which makes ε_1 turn from negative

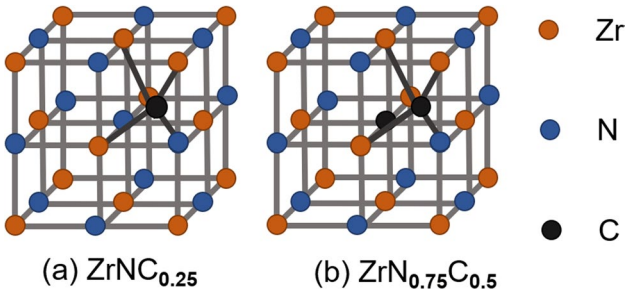

Fig. 12 Crystal cells of ZrC_xN_y with different interstitial C-doping $ZrNC_{0.25}$ (**a**) and mixed C-doping $ZrN_{0.75}C_{0.5}$ (**b**)

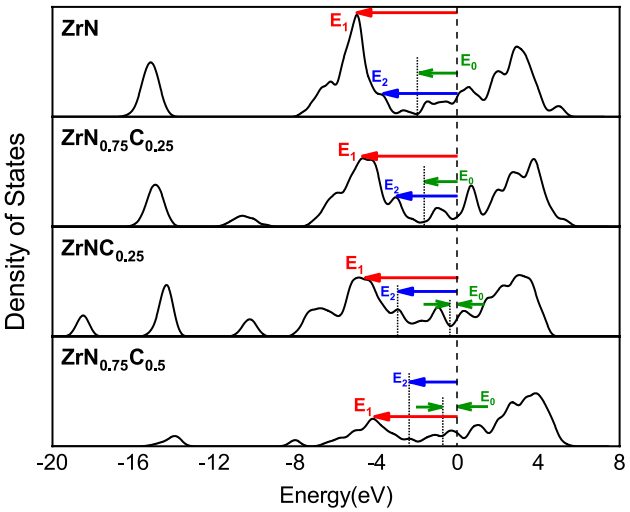

Fig. 13 Total density of states of ZrC_xN_y films with different C doping ways. Dashed lines represent Fermi levels

to positive at ω_c [50]. Above ω_c, the interband transition will make ε_1 a small positive value [50].

The electron transitions can be indicated by the characteristic energy levels E_0, E_1 and E_2 marked in Fig. 11 to a certain extent. At E_0, the total DOS reaches its minimum, and the hybridized 2*p* bands begins to dominate the DOS. The values of E_0 are approximatively equal to the $\hbar\omega_c$ values in Fig. 4. So E_0 can be regarded as the threshold energy of the dielectric contribution to the optical response. Obviously, E_0 value decreases as C content increases, which is similar to the experimental laws discussed above. For ZrC, E_0 is near fermi surface, which maybe leads to the dual epsilon-near-zero properties shown in Fig. 4. The characteristic energy E_1 and E_2 indicates the transition from the local maximum and the global maximum of the DOS of 2*p* bands to the fermi surface. Possibly, E_1 and E_2 are related to the local maximum of positive ε_1 and ε_2 in the short wavelength region (see Figs. 4, 7, and 9).

Besides the substitute doping, we calculated the DOS of the interstitial-C-doped ZrN. The calculation is based on the crystal cell of interstitial $ZrNC_{0.25}$, and $ZrN_{0.75}C_{0.5}$ with mixed (substitute and interstitial) doping, as shown in Fig. 12. The calculated corresponding DOS of ZrC_xN_y with interstitial and mixed doping are shown in Fig. 13. The DOS results of the undoped ZrN and substitute doping $ZrN_{0.75}C_{0.25}$ are also shown as contrast. The results show that effect of interstitial and mixed doping on the DOS is similar to substitute doping. Compared to the DOS of $ZrN_{0.75}C_{0.25}$, the valence bands of $ZrNC_{0.25}$ and $ZrN_{0.75}C_{0.5}$ shift more towards Fermi surface, and the characteristic energy are lower. There are possibly more interstitial C-related defects in the films prepared with high E_a and J_a.

5 Conclusions

ZrC_xN_y films with different carbon and nitrogen content were prepared with DIBD, in which the chemical content were modulated by flow ratio of the CH_4 and N_2. The structure and plasma properties of the films, and the effect of assisting ions were studied. The electronic state were studied with first principle calculation.

The XRD results show that a solid solution of fcc-ZrN and fcc-ZrC was obtained. All the films are (111)-oriented. With the increase of the C content, the lattice constant increases, and the crystal grain size decreases. As the incident wavelength increases, all the ZrC_xN_y films turn from dielectric to metallic. With the increase of carbon content, the screened plasma frequency $\hbar\omega_c$ and the carrier density *n* of the film decreases, and the maximum of the energy loss of the film shows a red shift. The energy E_a and current density J_a of assisting ion beam can give significant influence on the composition and plasmonic properties of the films. As E_a and J_a increases, $\hbar\omega_c$ and the *n* of the film initially increase, and then decrease. The behavior of plasmonic properties with E_a and J_a varying is related to the atomic composition. After all, as E_a and J_a increases, the carbon content of the film initially decreases, and then increases. The mechanism of C-doping affecting the permittivity is confirmed by the electronic states. The calculation of electronic DOS shows that carbon doping elevates the N-2*p* band and lowers the interband transition energy, and so lowers the screened plasma energy. Additionally, the C-doping defect type is another factor affecting the properties of the films.

The study shows that metal carbonitride is a kind of more tunable plasmonic material in visible and infrared region, and DIBD is an effective method to prepare and modulate the metal carbonitride films.

Acknowledgements This work was supported by the National Natural Science Foundation of China (No.11774029) and the Fundamental Research Funds for the Central Universities(FRF-TP-22-144A1). We thank Ms Le Zhao of National Center for Nanoscience and Technology for the ellipsometry measurement.

Declarations

Conflict of interest The authors declared that they do not have any commercial or associative interest that represents a conflict of interest in connection with the work submitted.

References

1. T. von Woedtke, S. Reuter, K. Masur, K.D. Weltmann, Plasmas for medicine. Phys. Rep. **530**, 291–320 (2013). https://doi.org/10.1016/j.physrep.2013.05.005
2. S. Bekeschus, P. Favia, E. Robert, T. von Woedtke, White paper on plasma for medicine and hygiene: Future in plasma health sciences. Plasma Process. Polym. **16**, 1800033 (2018). https://doi.org/10.1002/ppap.201800033
3. H.A. Atwater, A. Polman, Plasmonics for improved photovoltaic devices. Nat. Mater. **9**, 205–213 (2010). https://doi.org/10.1038/nmat2629
4. B. Anasori, M.R. Lukatskaya, Y. Gogotsi, 2D metal carbides and nitrides(MXenes) for energy storage. Nat. Rev. Mater. **2**, 16098 (2017). https://doi.org/10.1038/natrevmats.2016.98
5. B. Li, F. Zhang, W. Liu, X. Chen, Y. Gao, F. Wang, X. Zhang, X. Yan, T. Cheng, An ultraviolet sensor based on surface plasmon resonance in no-core optical fiber deposited by Ag and ZnO film. Surf. Interfaces **31**, 102074 (2022). https://doi.org/10.1016/j.surfin.2022.102074
6. D.D. Kumar, N. Kumar, S. Kalaiselvam, S. Dash, R. Jayavel, Wear resistant super-hard multilayer transition metal-nitride coatings. Surf. Interfaces **7**, 74–82 (2017). https://doi.org/10.1016/j.surfin.2017.03.001
7. S. Veprek, M.J.G. Veprek-Heijman, Industrial applications of superhard nanocomposite coatings. Surf. Coat. Technol. **202**, 5063–5073 (2008). https://doi.org/10.1016/j.surfcoat.2008.05.038
8. W.L. Barnes, A. Dereux, T.W. Ebbesen, Surface plasmon subwavelength optics. Nature **424**(6950), 824–830 (2003). https://doi.org/10.1038/nature01937
9. Z.L. Yu Li, C. Chi, H. Shan, L. Zheng, Z. Fang, Plasmonics of 2D nanomaterials: properties and applications. Adv. Sci. **4**, 1600430 (2017). https://doi.org/10.1002/advs.201600430
10. P.M.R. Yue-Jiao Zhang, X.-S. Zhou, H. Zhang, J.-L. Yao, J.-F. Li, Plasmonic core-shell nanomaterials and their applications in spectroscopies. Adv. Mater. **33**, 2005900 (2021). https://doi.org/10.1002/adma.202005900
11. T. Chung, C.S.H. Hwang, M.-S. Ahn, K.-H. Jeong, Au/Ag bimetallic nanocomposites as a highly sensitive plasmonic material. Plasmonics **14**, 407–413 (2018). https://doi.org/10.48550/arXiv.1806.10305
12. X. Fang, C.L. Mak, J. Dai, K. Li, H. Ye, C.W. Leung, ITO/Au/ITO sandwich structure for near-infrared plasmonics. ACS Appl. Mater. Interfaces **6**, 15743–15752 (2014). https://doi.org/10.1021/am5026165
13. M. Bomers, A. Mezy, L. Cerutti, F. Barho, F. Gonzalez-Posada Flores, E. Tourni, T. Taliercio, Phosphonate monolayers on InAsSb and GaSb surfaces for mid-IR plasmonics. Appl. Surf. Sci. **451**, 241–249 (2018). https://doi.org/10.1016/j.apsusc.2018.04.208
14. U. Guler, V.M. Shalaev, A. Boltasseva, Nanoparticle plasmonics: going practical with transition metal nitrides. Mater. Today **18**, 227–237 (2015). https://doi.org/10.1016/j.mattod.2014.10.039
15. G.V. Naik, J. Liu, A.V. Kildishev, V.M. Shalaev, A. Boltasseva, Demonstration of Al:ZnO as a plasmonic component for near-infrared metamaterials. Proc. Natl. Acad. Sci. **109**, 8834–8838 (2012). https://doi.org/10.1073/pnas.1121517109
16. G.V. Naik, J.L. Schroeder, X. Ni, A.V. Kildishev, T.D. Sands, A. Boltasseva, Titanium nitride as a plasmonic material for visible and near-infrared wavelengths. Opt. Mater. Express **2**, 478–489 (2012). https://doi.org/10.1364/OME.2.000478
17. G.V. Naik, V.M. Shalaev, A. Boltasseva, Alternative plasmonic materials: beyond gold and silver. Adv. Mater. **25**, 3264–3294 (2013). https://doi.org/10.1002/adma.201205076
18. P. Patsalas, N. Kalfagiannis, S. Kassavetis, G. Abadias, D.V. Bellas, C. Lekka, E. Lidorikis, Conductive nitrides: growth principles, optical and electronic properties, and their perspectives in photonics and plasmonics. Mater. Sci. Eng. R. Rep. **123**, 1–55 (2018). https://doi.org/10.1016/j.mser.2017.11.001
19. L. Zhang, H. Liu, X. Suo, S. Tong, Y. Li, Z. Jiang, Z. Wang, Plasmonic properties of titanium nitride thin films prepared by ion beam assisted deposition. Mater. Lett. **185**, 295–298 (2016). https://doi.org/10.1016/j.matlet.2016.08.147
20. L. Zhang, S. Tong, H. Liu, Y. Li, Z. Wang, Effects of sputtering and assisting ions on the orientation of titanium nitride films fabricated by ion beam assisted sputtering deposition from metal target. Mater. Lett. **171**, 304–307 (2016). https://doi.org/10.1016/j.matlet.2016.02.100
21. G.V. Naik, B. Saha, J. Liu, S.M. Saber, E.A. Stach, J.M. Irudayaraj, T.D. Sands, V.M. Shalaev, A. Boltasseva, Epitaxial superlattices with titanium nitride as a plasmonic component for optical hyperbolic metamaterials. Proc. Natl. Acad. Sci. **111**, 7546–7551 (2014). https://doi.org/10.1073/pnas.1319446111
22. J. Wang, W. Zhang, M. Zhu, K. Yi, J. Shao, Broadband perfect absorber with titanium nitride nano-disk array. Plasmonics **10**, 1473–1478 (2015). https://doi.org/10.1007/s11468-015-9962-x
23. W.M. Kima, S.H. Kimb, K.-S. Leea, T.S. Leea, I.H. Kim, Titanium nitride thin film as an adhesion layer for surface plasmon resonance sensor chips. Appl. Surf. Sci. **261**, 749–752 (2012). https://doi.org/10.1016/j.apsusc.2012.08.093
24. M.M. Larijani, M. Kiani, E. Jafari-Khamse, V. Fathollahi, Temperature dependence of the optical properties of ion-beam sputtered ZrN films. Appl. Phys. A **117**, 1179–1183 (2014). https://doi.org/10.1007/s00339-014-8495-z
25. H. Lu, Y. Ran, S. Zhao, L. Jia, C. Gao, Q. Guo, Z. Jiang, F. Yang, Z. Wang, Effects of assisting ions on the structural and plasmonic properties of ZrNx thin films. J. Phys. D Appl. Phys. **52**, 245102 (2019). https://doi.org/10.1088/1361-6463/ab10fe
26. A. Rizzo, M.A. Signore, L. Mirenghi, D. Dimaio, Deposition and properties of ZrNx films produced by radio frequency reactive magnetron sputtering. Thin Solid Films **515**, 1486–1493 (2006). https://doi.org/10.1016/j.tsf.2006.04.012
27. D. Valerini, M.A. Signore, A. Rizzo, L. Tapfer, Optical function evolution of ion-assisted ZrN films deposited by sputtering. J. Appl. Phys. **108**, 083536 (2010). https://doi.org/10.1063/1.3493267
28. L. Chen, Y. Ran, Z. Jiang, Y. Li, Z. Wang, Structural, compositional, and plasmonic characteristics of Ti-Zr ternary nitride thin films tuned by the nitrogen flow ratio in magnetron sputtering. Nanomaterials (Basel) **10**, 829 (2020). https://doi.org/10.3390/nano10050829
29. H. Lu, Y. Ran, S. Zhao, Q. Guo, C. Gao, Z. Jiang, F. Yang, Z. Wang, Modulation of the plasmonic characteristics of Ti-Zr ternary nitride thin films by assisting ions. Appl. Surf. Sci. **505**, 144579 (2020). https://doi.org/10.1016/j.apsusc.2019.144579
30. W. Tianrun, R. Yujing, L. Tingting, G. Qian, G. Chang, J. Zhaotan, W. Zhi, Plasmonic and electronic characteristics of (Zr, Nb)Nx thin films with different metal content. Appl. Phys. A (2022). https://doi.org/10.1007/s00339-022-05777-6
31. Y. Ran, H. Lu, S. Zhao, L. Jia, Y. Li, Z. Jiang, Z. Wang, Effects of substrate bias and temperature on the structure and dielectric properties of TiZrN ternary nitride thin films. Surf. Coat.

Technol. **359**, 258–264 (2019). https://doi.org/10.1016/j.surfcoat.2018.12.023
32. Jos D. Castro, M.J. Lima, S. Carvalho, Corrosion resistance of Cu-Zr(O)N films in a simulated seawater environment. Surf. Coat. Technol. **451**, 129050 (2022). https://doi.org/10.1016/j.surfcoat.2022.129050
33. L. Braic, N. Vasilantonakis, A. Mihai, I.J. Garcia, S. Fearn, B. Zou, N.M. Alford, B. Doiron, R.F. Oulton, S.A. Maier, A.V. Zayats, P.K. Petrov, Titanium Oxynitride Thin Films with Tunable Double Epsilon-Near-Zero Behavior for Nanophotonic Applications. ACS Applied Materials & Interfaces **9**, 29857–29862 (2017). https://doi.org/10.1021/acsami.7b07660
34. Q. Guo, T. Wang, Y. Ren, Y. Ran, C. Gao, H. Lu, Z. Jiang, Z. Wang, Plasmonic properties of nonstoichiometric zirconium nitride, oxynitride thin films, and their bilayer structures. Phys. Rev. Mater. **5**, 065201 (2021). https://doi.org/10.1103/PhysRevMaterials.5.065201
35. L. Jia, H. Lu, Y. Ran, S. Zhao, H. Liu, Y. Li, Z. Jiang, Z. Wang, Structural and dielectric properties of ion beam deposited titanium oxynitride thin films. J. Mater. Sci. **54**, 1452–1461 (2018). https://doi.org/10.1007/s10853-018-2923-y
36. E. Grigore, C. Ruset, X. Li, H. Dong, Zirconium carbonitride films deposited by combined magnetron sputtering and ion implantation (CMSII). Surf. Coat. Technol. **204**, 1889–1892 (2010). https://doi.org/10.1016/j.surfcoat.2009.11.012
37. A. Kenzhegulov, A. Mamaeva, A. Panichkin, Z. Alibekov, B. Kshibekova, N. Bakhytuly, W. Wieleb, Comparative study of tribological and corrosion characteristics of TiCN, TiCrCN, and TiZrCN coatings. Coatings **12**, 564 (2022). https://doi.org/10.3390/coatings12050564
38. M. Braic, V. Braic, M. Balaceanu, C.N. Zoita, A. Kiss, A. Vladescu, A. Popescu, R. Ripeanu, Structure and properties of Zr/ZrCN coatings deposited by cathodic arc method. Mater. Chem. Phys. **126**, 818–825 (2011). https://doi.org/10.1016/j.matchemphys.2010.12.036
39. C.L. Chu, H.L. Ji, C. Guo, X.B. Sheng, Y.S. Dong, P.H. Lin, T. Hu, P.K. Chu, Surface nanomechanical behavior of ZrN and ZrCN films deposited on NiTi shape memory alloy by magnetron sputtering. J. Nanosci. Nanotechnol. **11**, 11176–11180 (2011). https://doi.org/10.1166/jnn.2011.4051
40. R.W. Harrison, W.E. Lee, Processing and properties of ZrC, ZrN and ZrCN ceramics: a review. Adv. Appl. Ceram. **115**, 294–307 (2016). https://doi.org/10.1179/1743676115Y.0000000061
41. Z. Qi, P. Sun, Z. Wang, Microstructure and mechanical properties of TiCN coatings prepared by MTCVD. Adv. Tribol. **404**, 796–800 (2009). https://doi.org/10.1007/978-3-642-03653-8_263
42. J.H. Mokkath, Localized surface plasmon resonances and electric field confinement in titanium carbide (Ti3C2) MXene nanoclusters Phys. Chem. Chem. Phys. **23**, 25807 (2021). https://doi.org/10.1039/D1CP03960A
43. M. Gonçalves, A. Melikyan, H. Minassian, T. Makaryan, P. Petrosyan, T. Sargsian, Interband, surface plasmon and fano resonances in titanium carbide (MXene) nanoparticles in the visible to infrared range. Photonics **8**, 36 (2021). https://doi.org/10.3390/photonics8020036
44. Z. Jaksic, M. Obradov, D. Tanaskovic, O. Jaksic, D.V. Radovic, Electromagnetic simulation of MXene based plasmonic metamaterials with enhanced optical absorption. Opt. Quantum Electron. **52**, 83 (2020). https://doi.org/10.1007/s11082-020-2227-8
45. W. Hume-rothery, Comments on papers resulting from Hume-Rothery's Note-1965. Acta Metallur. **15**, 567–569 (1967). https://doi.org/10.1016/0001-6160%2867%2990091-0
46. Y. Ran, H. Lu, S.A. Zhao, Q. Guo, C. Gao, Z. Jiang, Z. Wang, Stoichiometry-modulated dual epsilon-near-zero characteristics of niobium nitride films. Appl. Surf. Sci. **537**, 147981 (2021). https://doi.org/10.1016/j.apsusc.2020.147981
47. G.V. Naik, J. Kim, A. Boltasseva, Oxides and nitrides as alternative plasmonic materials in the optical range. Opt. Mater. Express **6**, 1090–1099 (2011). https://doi.org/10.1364/OME.1.001090
48. Y. Wang, A. Capretti, L. Dal Negro, Wide tuning of the optical and structural properties of alternative plasmonic materials. Opt. Mater. Express **5**, 2415–2430 (2015). https://doi.org/10.1364/OME.5.002415
49. S. Adachi, M. Takahashi, Optical properties of TiN films deposited by direct current reactive sputtering. J. Appl. Phys. **87**, 1264–1269 (2000). https://doi.org/10.1063/1.372006
50. A. Catellani, A. Calzolari, Plasmonic properties of refractory titanium nitride. Phys. Rev. B (2017). https://doi.org/10.1103/PhysRevB.95.115145

Publisher's Note Springer Nature remains neutral with regard to jurisdictional claims in published maps and institutional affiliations.

Springer Nature or its licensor (e.g. a society or other partner) holds exclusive rights to this article under a publishing agreement with the author(s) or other rightsholder(s); author self-archiving of the accepted manuscript version of this article is solely governed by the terms of such publishing agreement and applicable law.